Supplementary Information for

Projected Reversal of Oceanic Stable Carbon Isotope Ratio Depth Gradient with Continued Anthropogenic Carbon Emissions

Eun Young Kwon[1,2]*, Axel Timmermann[1,2], Brett, J. Tipple[3], Andreas Schmittner[4]

[1] Center for Climate Physics, Institute for Basic Science, Busan, 46241, South Korea.

[2] Pusan National University, Busan, 46241, South Korea.

[3] School of Biological Sciences, University of Utah, Salt Lake City, UT 84112, USA.

[4] College of Earth, Ocean, and Atmospheric Sciences, Oregon State University, Corvallis, OR 97331-5503, USA.

* Corresponding author: Eun Young Kwon (ekwon957@gmail.com)

This PDF file includes:

Supplementary Note 1: Carbon Cycle Model Formulations

Here, we present the details of model formulations and identify the model parameters that are varied in our Monte Carlo experiment. Specifically, we consider the following sources of uncertainty: (A) preindustrial $\delta^{13}C$ values for atmospheric CO_2, (B) thermodynamic equilibrium fractionation factors for air-sea CO_2 exchange and the historical changes in sea surface temperature, (C) the globally uniform $\delta^{13}C$ values of riverine carbon inputs of dissolved organic carbon (DOC), particulate organic carbon (POC), dissolved inorganic carbon (DIC), (D) the magnitude of non-riverine terrestrial carbon inputs, (E) the air-sea CO_2 exchange rates, (F) fractionation factors for the photosynthetic uptake of carbon, (G) ocean mixing and circulation states, and (H) the magnitude of inorganic carbon buried in marine sediments. Those are varied over the ranges summarized in Supplementary Table 1, and represented by the parameters f1-f10 as shown below. We note that the same model formulations are also presented in the Supplementary Materials of Kwon, et al. [1].

The stable carbon isotope ^{13}C is a prognostic variable in the model. The $\delta^{13}C$ of DIC is calculated using the simulated $DI^{13}C$ and $DI^{12}C$ as $\delta^{13}C\text{-}DIC = [(DI^{13}C/DI^{12}C)_{sample}/(DI^{13}C/DI^{12}C)_{standard} - 1]$ with the Vienna Pee Dee Belemnite standard. We do not distinguish $DI^{12}C$ from DIC in the model, because $DI^{12}C$ accounts for 98.9% of DIC. The governing equation for the $DI^{12}C$ model is

$$\frac{\partial[\mathrm{DI}^{12}\mathrm{C}]}{\partial t} + U \cdot \nabla[\mathrm{DI}^{12}\mathrm{C}] - \nabla\left(K\nabla[\mathrm{DI}^{12}\mathrm{C}]\right) = Jv_{DI^{12}C} + Jg_{DI^{12}C} + Jb_{DI^{12}C} + Jt_{DI^{12}C} + Jl_{DI^{12}C}, \quad \text{(S1)}$$

where the three terms on the left-hand side represent the time rate of change in $DI^{12}C$, and the advective and mixing processes of $DI^{12}C$. The five terms on the right-hand side represent the concentrating and diluting effect due to evaporation and precipitation (*Jv*), the air-sea gas exchange (*Jg*), the biological source and sink (*Jb*), the terrestrial carbon inputs to the ocean (*Jt*), and the sedimentary burial loss (*Jl*). The gas exchange term is expressed as

$$Jg_{DI^{12}C} = -(1 - Fice) \cdot k_g \cdot {z_0}^{-1} \cdot \left([^{12}\mathrm{CO}_2] - [^{12}\mathrm{CO}_2^{\mathrm{sat}}]\right), \quad \text{(S2)}$$

where *Fice* is a fraction of sea surface covered by sea ice, z_0 = 36 m is the thickness of the ocean top layer in the model, and $[^{12}CO_2]$ is simulated aqueous $^{12}CO_2$ concentration at the sea-surface and $[^{12}CO_2^{sat}]$ is saturated aqueous $^{12}CO_2$ concentration, the latter that is computed by multiplying the atmospheric pCO_2 (in μatm) with the solubility of CO_2 in seawater k_0 (in mol m^{-3} μatm^{-1}). The air-sea CO_2 transfer velocity k_g (in ms^{-1}) is formulated following an equation [2] adopted in the second phase of the Ocean Carbon Model Intercomparison Project (OCMIP2) protocol [3] as

$$k_g = f1 \cdot \overline{u^2} \cdot (Sc/660)^{-1/2}, \quad \text{(S3)}$$

where *f1* is a linear scaling factor for the CO_2 transfer velocity, *u* is the daily mean wind speed, an overbar represents a temporal average, and *Sc* is the Schmidt number. The scaling factor *f1* is varied such that the globally-integrated k_g ranges from 13.0 cm/hr to 17.0 cm/hr (ref. [4-7]).

The biological source and sink terms are based on the OCMIP2 protocol [3], and consist of the biological production and remineralization of organic carbon (OC) and $CaCO_3$ as

$$Jb_{DI^{12}C} = Jb_{O^{12}C} + Jb_{Ca^{12}CO3}. \quad \text{(S4)}$$

We refer readers to Kwon and Primeau [8] for the detailed descriptions of the *Jb* terms and the $DI^{12}C$ cycle model. The *Jb* term is important for bringing our simulated tracer distributions close to observations. Therefore, we optimize the model parameters governing the biological source and sink terms against the observed PO_4, alkalinity, and $DI^{12}C$ [9,10] using the same method employed in Kwon and Primeau [8], prior to the Monte Carlo experiment.

The terrestrial carbon input *Jt* term includes dissolved organic carbon (DOC) fluxes from rivers, particulate organic carbon (POC) fluxes from rivers and aerosols, and DIC fluxes from rivers and coastal margins as follows:

$$Jt_{DI^{12}C} = \frac{1}{\tau} \cdot [\mathrm{DOCr}] + Jt_{POC} + Jt_{DIC}, \quad \text{(S5)}$$

where DOCr is DOC from rivers, τ is the lifetime of DOCr and fixed at 8 years [11], and Jt_{POC} combines the riverine and aerosol driven POC fluxes, assumed to be remineralized instantaneously to DIC at the ocean bottom layer of the river mouths and the aerosol deposition sites, respectively. DOCr is the solution of the equation of

$$\frac{\partial[\mathrm{DOCr}]}{\partial t} + U \cdot \nabla[\mathrm{DOCr}] - \nabla(K\nabla[\mathrm{DOCr}]) = Jt_{DOC} - \frac{1}{\tau} \cdot [\mathrm{DOCr}], \quad \text{(S6)}$$

where Jt_{DOC} is riverine DOC flux. Jt_{DOC} and Jt_{POC} are prescribed using the Global Nutrient Export from Watersheds (NEWS2) model [12] for riverine fluxes and the atmospheric model constrained by observations [13] for aerosol driven fluxes. Jt_{DIC} includes DIC fluxes from rivers (Jt_{DIC_river}) and coastal margins (Jt_{DIC_CM}), the latter including fluxes through submarine groundwater discharge and direct lateral inputs from coastal vegetation. While riverine DIC fluxes are prescribed using the GEMS-GLORI database [14], the magnitude and geographic distributions for the coastal margin DIC inputs are highly uncertain. Thus, Jt_{DIC_CM} is parameterized as

$$Jt_{DIC\_CM} = f2 \cdot fCM, \quad \text{(S7)}$$

where *fCM* is a globally uniform DIC flux within the top 217 m around the global coastlines except Antarctica and *f2* is varied such that the globally integrated Jt_{DIC_CM} ranges from 0 to 1.4 GtC/yr (refs. [15,16]). Once discharged to the ocean, the coastal margin DIC mixes with oceanic DIC and undergoes transport by ocean circulation, air-sea CO_2 exchange, biological cycling, and sedimentary burial.

The sedimentary burial flux *Jl* term is parameterized using another parameter *f3* as

$$Jl_{DI^{12}C} = \begin{cases} -f3 \cdot fburial & \text{where } \Omega \geq 1 \\ 0 & \text{where } \Omega < 1 \end{cases}, \quad \text{(S8)}$$

where *fburial* is a uniform DIC sink from the ocean bottom layer, and the saturation state of seawater with respect to calcite, Ω, is determined using the GLODAPv2 dataset [9]. The scaling factor *f3* is chosen such that the globally integrated burial rate of inorganic carbon is bounded by 0.1-0.3 GtC/yr (ref. [17,18]).

In the following, we describe our DI^{13}C model equations. The governing equation for DI^{13}C can be written as

$$\frac{\partial[\mathrm{DI}^{13}\mathrm{C}]}{\partial t} + U \cdot \nabla[\mathrm{DI}^{13}\mathrm{C}] - \nabla(K\nabla[\mathrm{DI}^{13}\mathrm{C}]) = Jv_{DI^{13}C} + Jg_{DI^{13}C} + Jb_{DI^{13}C} + Jt_{DI^{13}C} + Jl_{DI^{13}C}, \quad \text{(S9)}$$

where $Jb_{DI^{13}C} = Jb_{O^{13}C} + Jb_{Ca^{13}CO3}$. The virtual flux term ($Jv_{DI^{13}C}$) only redistributes surface DI^{13}C, the same way as ocean circulation does. Hence, the virtual flux term can be treated as the ocean transport term on the left-hand side, representing the convergence and divergence of DI^{13}C due to ocean circulation and air-sea freshwater fluxes.

The fractionation during air-sea gas exchange is expressed as

$$Jg_{DI^{13}C} = -f1 \cdot \frac{k_g}{z_0} \alpha_k \left(\alpha_{aq \leftarrow DIC} \cdot \frac{[DI^{13}C]}{[DI^{12}C]} \cdot [{}^{12}CO_2] - \alpha_{aq \leftarrow g} \cdot \frac{{}^{13}CO_2^{air}}{{}^{12}CO_2^{air}} \cdot [{}^{12}CO_2^{sat}] \right), \quad \text{(S10)}$$

where α_k is the kinetic fractionation factor, $\alpha_{aq \leftarrow DIC}$ is the fractionation factor from DIC to aqueous CO_2, $\alpha_{aq \leftarrow g}$ is the fractionation factor from gaseous CO_2 to aqueous CO_2, and CO_2^{air} is atmospheric CO_2 concentration. The kinetic fractionation factor and the fractionation factor from gaseous to aqueous

CO_2 are fixed at α_k=0.99915 and $\alpha_{aq\leftarrow g}$ =0.998764, respectively [19]. The fractionation factor $\alpha_{aq\leftarrow DIC}$ can be rewritten as $\alpha_{aq\leftarrow DIC}=\alpha_{aq\leftarrow g}/\alpha_{DIC\leftarrow g}$ with $\alpha_{DIC\leftarrow g} = 1.4\times10^{-5}\cdot T\cdot f_{CO3} - 1.05\times10^{-4}\cdot T + f5$, *where f5* is varied within *1.01053±0.00005, T* is ocean temperature in °C, and fco_3 is the fraction of CO_3^{2-} ions in DIC [20]. Three different observation-based estimates of *T* are used over 1870-2018 (refs. [21-23]), whereas the temporal averages over the first 50 years are used over 1780-1869.

The fractionation during the photosynthetic fixation of CO_2 is expressed as

$$Jb_{O^{13}C} = \alpha_{OC\leftarrow DIC}\cdot\frac{[DI^{13}C]}{[DI^{12}C]}\cdot Jb_{O^{12}C}, \quad \text{(S11)}$$

where $\alpha_{OC\leftarrow DIC}$ is the fractionation factor from DIC to organic carbon, which includes both particulate and dissolved organic carbon. The fractionation factor from DIC to organic carbon can be rewritten as $\alpha_{OC\leftarrow DIC}=\alpha_{OC\leftarrow aq}\cdot\alpha_{aq\leftarrow g}/\alpha_{DIC\leftarrow g}$ with $\alpha_{OC\leftarrow aq} = f6\cdot log_{10}([CO_2]) + f7$ where $[CO_2]$ is aqueous CO_2 concentration in μmol l^{-1}, and the coefficients *f6* and *f7* are randomly chosen from three different sets suggested by Goericke and Fry [24], Popp, et al. [25], and Freeman and Hayes [26] (Supplementary Table 1). This parameterization gives the photosynthetic fractionations from DIC to organic carbon ranging from –(16~18)‰ in low latitudes to –(27~29)‰ in high latitudes, which also temporally change with increasing CO_2 concentrations. There is no fractionation during the formation and dissolution of biogenic $CaCO_3$, and hence the $Jb_{Ca^{13}CO3}$ term becomes

$$Jb_{Ca^{13}CO3} = Jb_{Ca^{12}CO3}\cdot\frac{[DI^{13}C]}{[DI^{12}C]}. \quad \text{(S12)}$$

The $\delta^{13}C$ endmember values for riverine carbon are chosen from the ranges of *f8* = –27±2‰ for DOC, *f9* = –30±2‰ for POC, and *f10* = –15±2‰ for DIC [27,28]. For the coastal margin carbon flux, the $\delta^{13}C$ endmember value is fixed at –26‰ [29,30]. Although the $\delta^{13}C$ values for the riverine and coastal margin inputs are highly uncertain spanning –(14-30)‰ [29,30], its uncertainty is implicitly included in our Monte Carlo experiment because the effects on the $\delta^{13}C$-DIC are identical between the magnitude of the coastal margin inputs (*f2*) and the $\delta^{13}C$ values of the riverine or coastal margin inputs. The term representing terrestrial $DI^{13}C$ inputs becomes

$$Jt_{DI^{13}C} = (1+f8/1000)\cdot\frac{1}{\tau}\cdot[DOCr] + (1+f9/1000)\cdot Jt_{POC} + (1+f10/1000)\cdot Jt_{DIC_{river}} + 0.974\cdot Jt_{DIC\_CM}. \quad \text{(S13)}$$

Fractionation does not occur during the sedimentary burial of $DI^{13}C$, hence

$$Jl_{DI^{13}C} = \begin{cases} -f3\cdot fburial\cdot\frac{[DI^{13}C]}{[DI^{12}C]} & \text{where } \Omega \geq 1 \\ 0 & \text{where } \Omega < 1 \end{cases}. \quad \text{(S14)}$$

A circulation field is also randomly selected from a suite of 10 ocean circulation fields [31]. With slightly different ocean mixing parameterizations and data-assimilation methods, the suite of circulation models is designed to cover the uncertainty of the present-day climatological mean ocean circulation within the inverse modeling framework [31,32]. The model density structure and circulation are very close

across the circulation fields with Atlantic overturning rates of 20±1 Sv (1 Sv = 10^6 m^3/s), Southern Ocean overturning rates of 16±1 Sv, and Drake Passage transport of 151±3 Sv [33]. Nonetheless, the deep ocean ventilation age (defined as the time that has elapsed since the water was last in contact with the atmosphere) averaged at 2-3 km depths ranges from 687 years to 777 years, which is roughly scaled with three different horizontal maxing coefficients (600 m^2/s, 1000 m^2/s, and 2000 m^2/s) imposed in the model. The slight differences in ocean circulation result in slight differences in ocean surface productivity and the subsequent remineralization, due to different supply rates of PO_4 and nutrient availability in the euphotic zone.

Supplementary Note 2: Uncertainty in Historical δ^{13}C-DIC Changes (from a year 1780 to 2018)

The simulated oceanic ^{13}C Suess effect is predominantly controlled by anthropogenic perturbations rather than initial states of oceanic δ^{13}C-DIC prior to the perturbations. Among the sources of uncertainties considered in our Monte Carlo simulations (Supplementary Table 1), uncertainties in the air-sea CO_2 piston velocity [5,7] and the atmospheric ^{13}C Suess effect [34] explain 84% of the total uncertainty with contributions of 43% and 41%, respectively (Supplementary Fig. 1a). A greater air-sea CO_2 piston velocity leads to a greater depletion of the δ^{13}C-DIC for the global ocean, through its influence on the oceanic uptake of anthropogenic CO_2 and enhanced exchange rates of $^{13}C/^{12}C$. A higher preindustrial atmospheric δ^{13}C of CO_2, leading to a greater atmospheric ^{13}C Suess effect, also causes a greater ^{13}C-depletion of the oceanic δ^{13}C-DIC through a more negative isotopic signature of anthropogenic CO_2. The other sources of uncertainties, including the terrestrial carbon inputs, ocean circulation, isotope fractionation factors during photosynthesis and air-sea CO_2 exchange, and the fraction of terrestrial carbon buried into marine sediments, also contribute little to the estimated uncertainty in the oceanic ^{13}C Suess effect (Supplementary Fig. 1). On the other hand, ocean circulation are of the first order importance for the oceanic inventory of anthropogenic DIC. The distinct sources of uncertainty for the anthropogenic DIC and δ^{13}C-DIC simulations are broadly consistent with a previous study [35] based on an Earth System Model. This distinction can be attributed to distinct rate limiting steps for the oceanic uptake of anthropogenic CO_2 and δ^{13}C-CO_2, which have been identified as the surface-subsurface water exchange rates for CO_2 and air-sea gas exchange for δ^{13}C-CO_2 (ref. [5]).

Supplementary Note 3: Uncertainty in Future δ^{13}C-DIC Changes (from a year of 2019 to 2100)

The primary source of uncertainty for the 21st century projection is likely future atmospheric ^{13}C Suess effect, which yields an averaged surface δ^{13}C-DIC excursion of –(1.8 to 6.3)‰ by the end of the 21st century. To explore potential uncertainty arising from our neglect of future changes in air-sea CO_2 exchange rates, and sea surface temperature (SST) and salinity (SSS), we use temporally and spatially varying estimates based on the Community Earth System Model version 2 (CESM2) [36]. Specifically, we use the Large Ensemble Simulations based on the CESM2 where the fully coupled climate model is run

using a historical greenhouse gases forcing from 1850 to 2014, and the SSP3-7.0 forcing from 2015 to 2100, with 100 different initial conditions [37].

In order to incorporate the CESM2-based climate change simulations into our offline ocean model framework, we first interpolate the annual mean fields of the fraction of sea surface covered by sea ice, SST, SSS, and 10 m wind speed, obtained from the CESM2 Large Ensemble Simulations, into our model grid cells. Secondly, we take the ensemble averages of 100 members and scale (normalize) the temporal evolutions from 2019 to 2100 with respect to the respective 2000-2018 temporal averages for each grid cell. The relative changes with respect to the 2000-2018 averages, which vary across the model grid cells, are then used to compute the following three terms for a simulation over 2019-2100: (i) air-sea CO_2 exchange rate of $(1 - Fice) \cdot \overline{u^2} \cdot (Sc/660)^{-1/2}$ in Equation (S2), (ii) CO_2 solubility in seawater, and (iii) the temperature dependent thermodynamic equilibrium fractionation factor [20]. The use of an ensemble average for each variable allows us to impose anthropogenically forced changes to our offline ocean model, rather than imposing simulated natural variability. The normalization with respect to the 2000-2018 temporal averages ensures a seamless simulation from 1780 to 2100 while taking into account climate change effects on the projected oceanic ^{13}C Suess effect.

For the CESM2-based projection, we use the full model setup for a simulation from 1780 to 2018. For a simulation from 2019 to 2100, we use the three terms (i), (ii), and (iii) listed above, and run the model from 2019 to 2100 under the RCP6.0 scenario (which is similar to the SSP3.7-0). A difference of $\delta^{13}C$-DIC between the CESM2-based projection and the projection based on the full model setup can be interpreted as the net effect of changing air-sea CO_2 exchange rates, SST, and SSS on the oceanic ^{13}C Suess effect. The net effect also includes the effect of changing thermodynamic equilibrium fractionation through changing SST. We additionally quantify the effect of changing thermodynamic equilibrium fractionation only by applying the CESM2-derived SST changes for the term (iii) while fixing the other two terms (i) and (ii) at those obtained from the full model setup. A difference from the projection based on the full model setup can be interpreted as the effect of changing thermodynamic equilibrium fractionation on the oceanic ^{13}C Suess effect.

The combined effects from changing air-sea CO_2 exchange rates, SST, and SSS on the 21st century oceanic ^{13}C Suess effect are shown in Supplementary Figs. 4 and 5. Overall, the changing air-sea CO_2 exchange rates, SST, and SSS in a warming climate, has an impact on further decreasing surface $\delta^{13}C$-DIC. In particular, the most pronounced differences of up to –0.4 ‰ as of 2100 are found at high latitudes where sea ice melting increases air-sea CO_2 exchange rates (Supplementary Figs. 5c and 5d). Increasing SST in a major fraction of the global ocean surface also enhances the thermodynamic equilibrium fractionation, whose effects are most pronounced in relatively well-equilibrated subtropical gyres (Supplementary Figs. 5e and 5f). The perturbation ratio of surface ocean $\delta^{13}C$-DIC to atmospheric $\delta^{13}C$-CO_2 also increases accordingly by up to 0.1. Nevertheless, the climate driven modulations of the

oceanic ^{13}C Suess effect are an order of magnitude smaller than the geochemically driven ^{13}C Suess effect that ranges from –(1 to 5) ‰ spatially (Supplementary Figs. 5a and 5b).

We provide upper and lower bounds of the CESM2-based projection, consistent with those from our Monte Carlo experiment. For this, we run two CESM2-based experiments: an upper bound simulation where the CESM2-based projection is combined with a pre-2019 simulation of a globally averaged air-sea CO_2 transfer velocity of 17.0 cm/hr and a preindustrial atmospheric $\delta^{13}C\text{-}CO_2$ of –6.3 ‰, and a lower bound simulation where the CESM2-based projection is combined with a pre-2019 simulation of a globally averaged air-sea CO_2 transfer velocity of 13.0 cm/hr and a preindustrial atmospheric $\delta^{13}C\text{-}CO_2$ of -6.5 ‰. These two simulations bracket the CESM2-based projection combined with a full model setup (with a globally averaged air-sea CO_2 transfer velocity of 15.1 cm/hr and a preindustrial atmospheric $\delta^{13}C\text{-}CO_2$ of –6.5 ‰) (Supplementary Table 1). The range of the globally averaged surface ocean ^{13}C Suess effect obtained from these two simulations is 0.3 ‰ as of 2018, which overlaps with 0.3 ‰ obtained from the Monte Carlo experiment (Supplementary Fig. 4). A range of 0.6 ‰ for a year of 2100 (Supplementary Fig. 4) is about an order of magnitude smaller than the scenario uncertainty of 4.5‰.

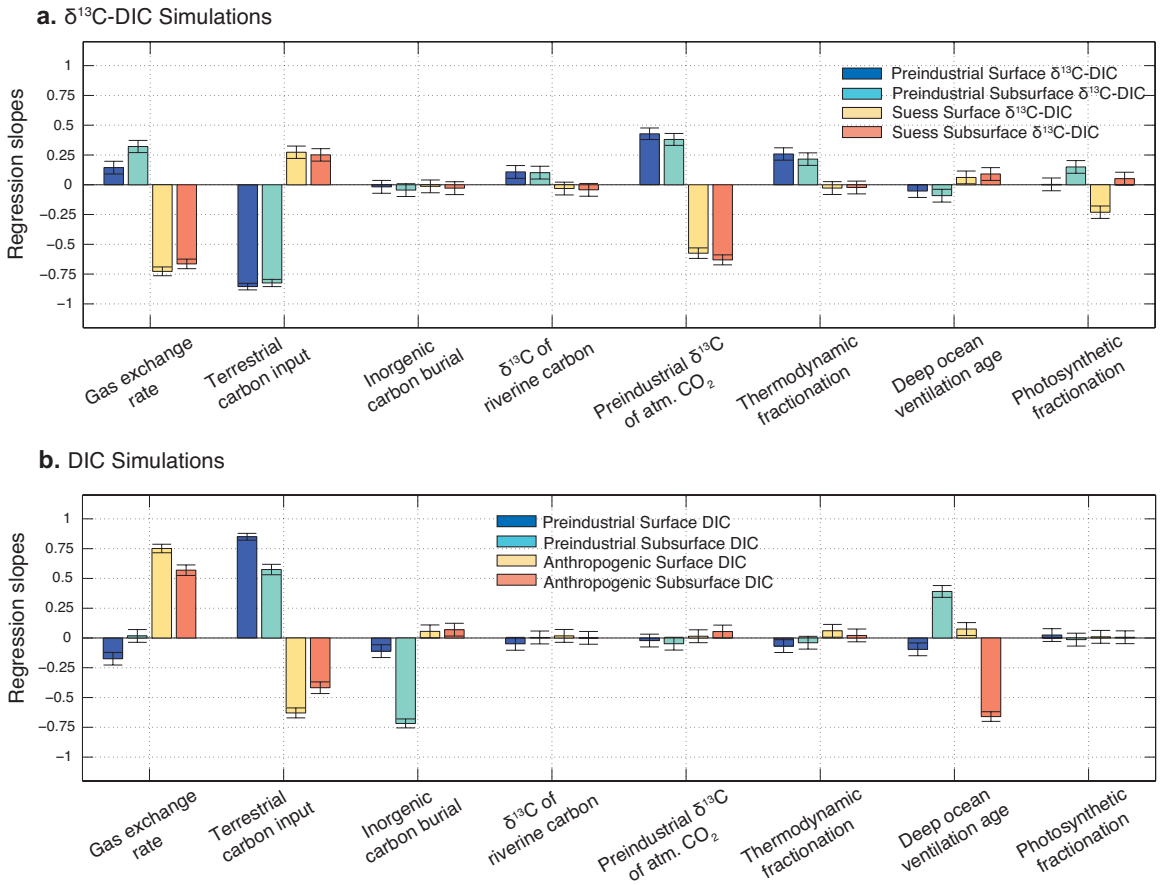

Supplementary Figure 1 Sources of uncertainty and their relative contributions to the estimated uncertainty. Different sources of uncertainty are shown in X-axes. Linear regression slopes between model-based estimates (denoted as different color bars) and input variables (Supplementary Table 1), estimated using 1400 simulations, are shown in Y-axes. Both the model estimates and input variables are standardized by dividing a departure from its mean value by a standard deviation prior to regression. Therefore, there are no units for the regression slopes. (a) Model estimates include the preindustrial surface-averaged δ^{13}C-DIC (dark blue), preindustrial subsurface-averaged δ^{13}C-DIC (light blue), surface-averaged ^{13}C Suess effect (yellow), subsurface-averaged ^{13}C Suess effect (red). The error bars represent 95 % confidence intervals. (b) Same as (a) except that regression slopes are obtained for the preindustrial surface-averaged DIC (dark blue), preindustrial subsurface-averaged DIC (light blue), surface-averaged anthropogenic DIC (yellow), subsurface-averaged anthropogenic DIC (red). Here "subsurface" is defined as water below a depth of 74 m.

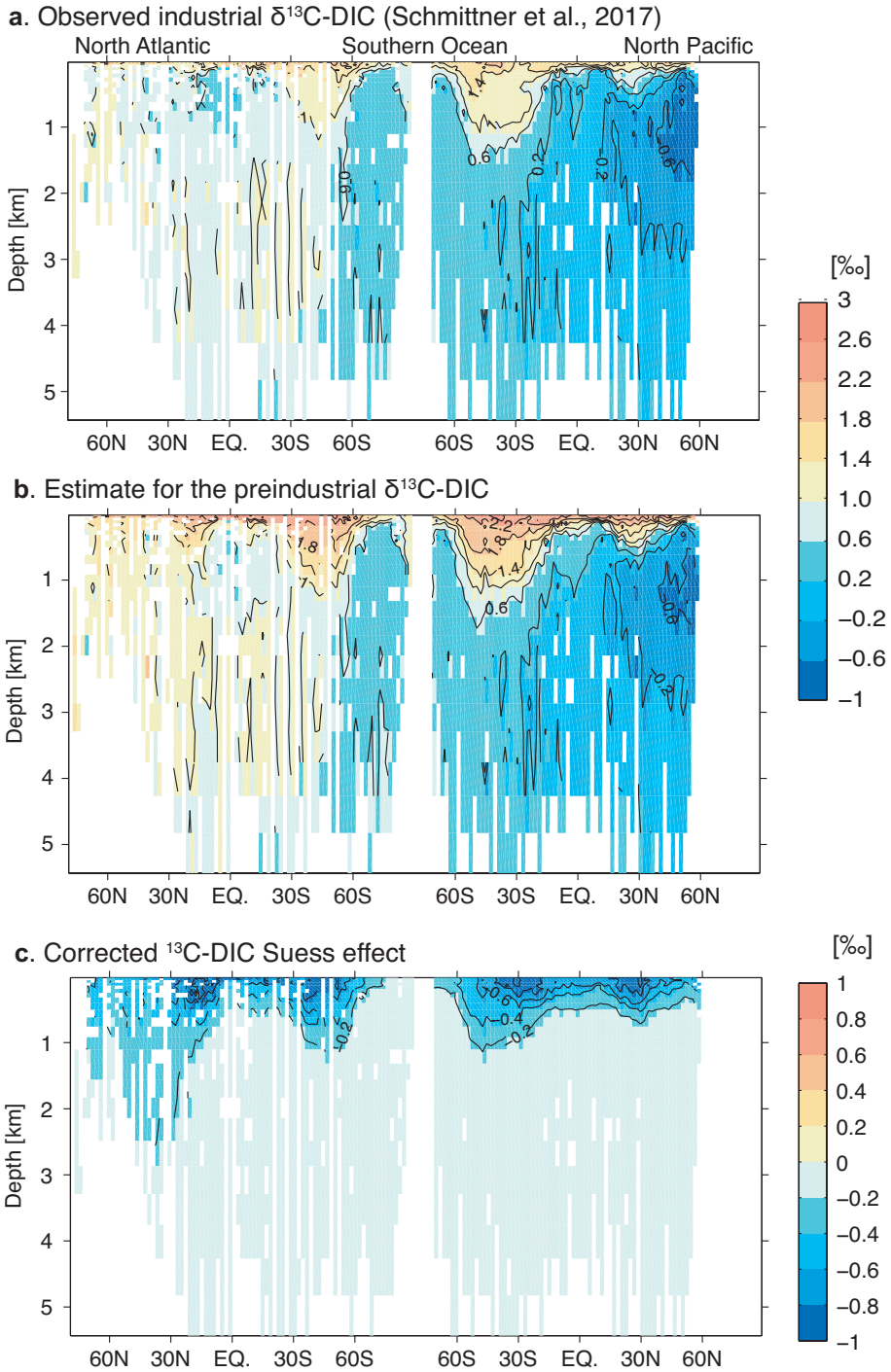

Supplementary Figure 2 Observed and estimated δ^{13}C-DIC. (a) The modern ocean observed δ^{13}C-DIC [38] gridded into the model grid cells, showing the zonally-averaged vertical section from the North Atlantic through the Southern Ocean to the North Pacific. The observation period is 1972-2016 and the temporally averaged values are shown. (b) Our estimated preindustrial δ^{13}C-DIC, obtained by subtracting the estimated ^{13}C Suess effect (shown in (c)) from the observations (a). Also shown in Fig. 2b. (c) The ^{13}C Suess effect averaged over an observation period for each grid cell, which is applied to the contemporary observations to correct for the ^{13}C Suess effect to derive a preindustrial distribution shown in (b).

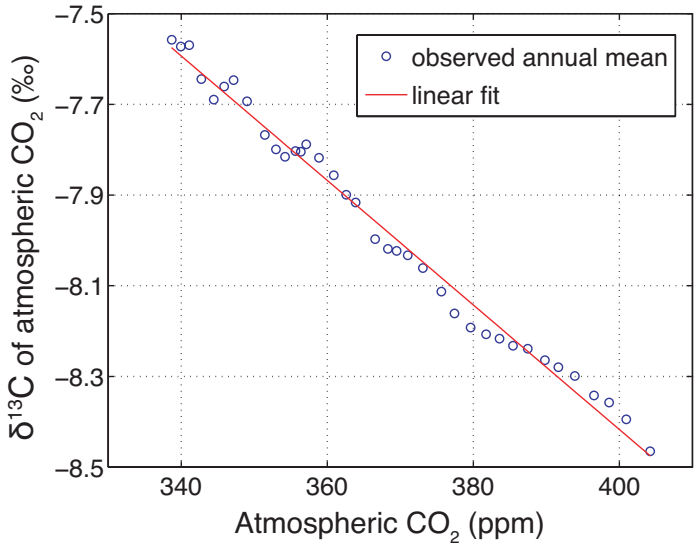

Supplementary Figure 3 The relationship between atmospheric CO_2 and the $\delta^{13}C$ of atmospheric CO_2 derived from the observations over 1980-2015 (ref. [39]). Annual mean values are shown in blue circles. The red line is a linear fit to the blue circles with an equation of $\delta^{13}C\text{-}CO_2 = -2.9 - 0.014 \times [CO_2]$ where $\delta^{13}C\text{-}CO_2$ is the $\delta^{13}C$ of atmospheric CO_2 in ‰ and $[CO_2]$ is atmospheric CO_2 concentration in ppm. The linear fit is used to project the $\delta^{13}C$ of atmospheric CO_2 from 2019 to 2100 based on the projected atmospheric CO_2 concentrations.

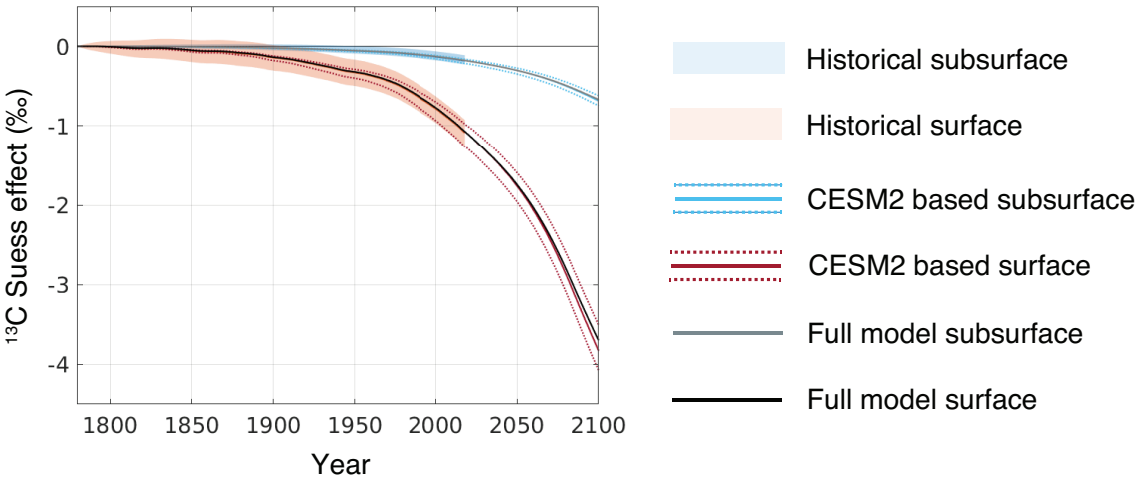

Supplementary Figure 4 The subsurface and surface averaged ^{13}C Suess effect simulated under the RCP6.0 scenario. The blue and red shades show the historical simulations based on the Monte Carlo experiment as shown in Fig. 1a. The gray and black solid lines show the estimates from the full model setup where time-invariant air-sea CO_2 exchange rates, and sea surface temperature and salinity are used throughout the simulation. The blue and red solid lines show the Community Earth System Model version 2 (CESM2) based estimates where we use temporally varying fields of air-sea CO_2 exchange rates, and sea surface temperature and salinity from 2019 to 2100 (obtained from the CESM2 Large Ensemble Simulations [37]) instead of the time-invariant fields of the full model setup. The blue and red dotted lines show the upper and lower bounds of the CESM2-based estimates, and take into account the uncertainty in the present-day air-sea CO_2 exchange rates and the historical atmospheric ^{13}C Suess effect.

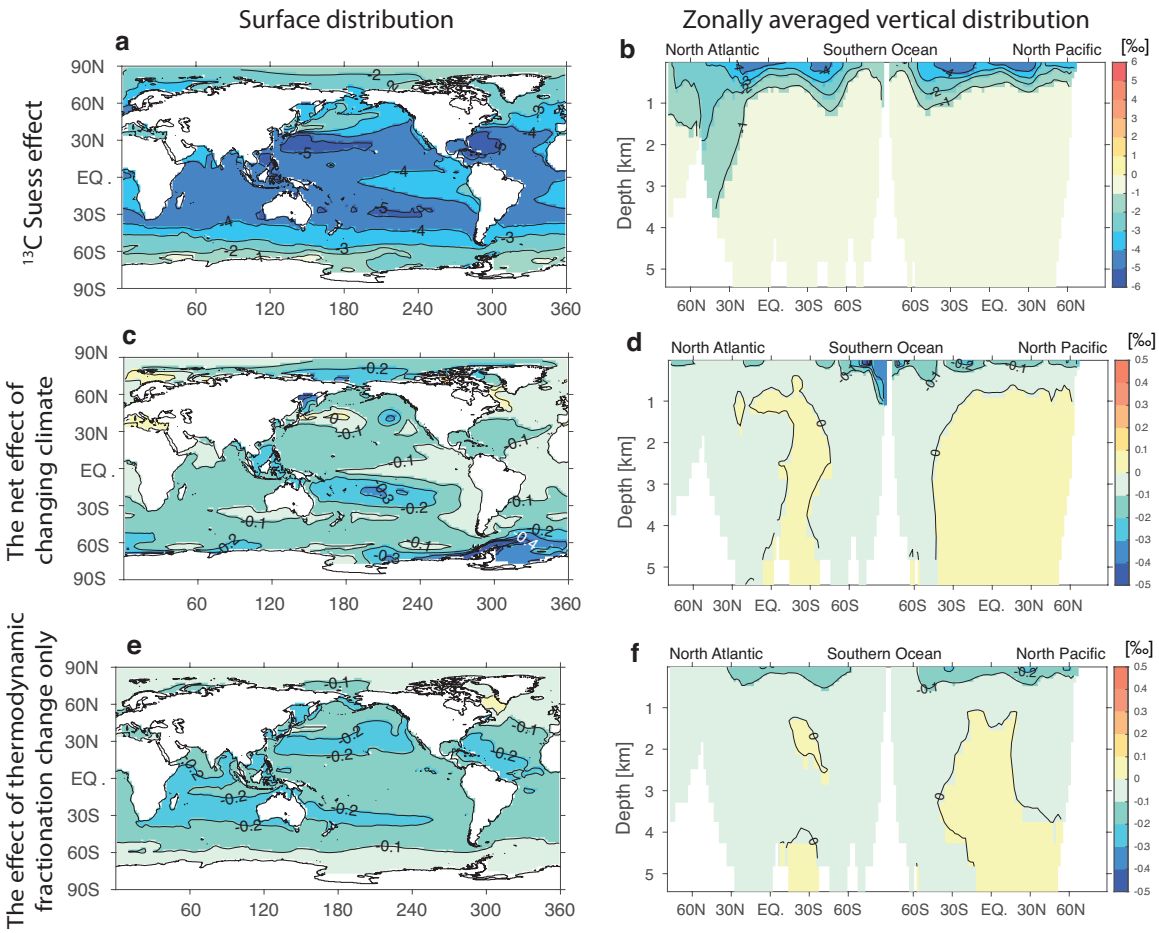

Supplementary Figure 5 The CESM2-based estimates for the ocean ^{13}C Suess effect as of 2100 projected under the RCP6.0 scenario. (a and b) The oceanic ^{13}C Suess effect simulated by allowing the air-sea CO_2 exchange rates, sea surface temperature and salinity to vary with time (2019-2100) according to the CESM2 Large Ensemble Simulation [37]. (a) Surface distribution as of 2100. (b) the zonally averaged vertical section from the North Atlantic to the Southern Ocean, and to the North Pacific as of 2100. (c and d) The net effect of time-varying air-sea CO_2 exchange rates, sea surface temperature and salinity on the projected oceanic ^{13}C Suess effect, i.e., the CESM2-based simulation shown in (a) minus the full model setup. (e and f) The effect of time-varying thermodynamic equilibrium ^{13}C fractionation only. A simulation where the thermodynamic equilibrium ^{13}C fractionation only is allowed to vary with time minus the full model setup.

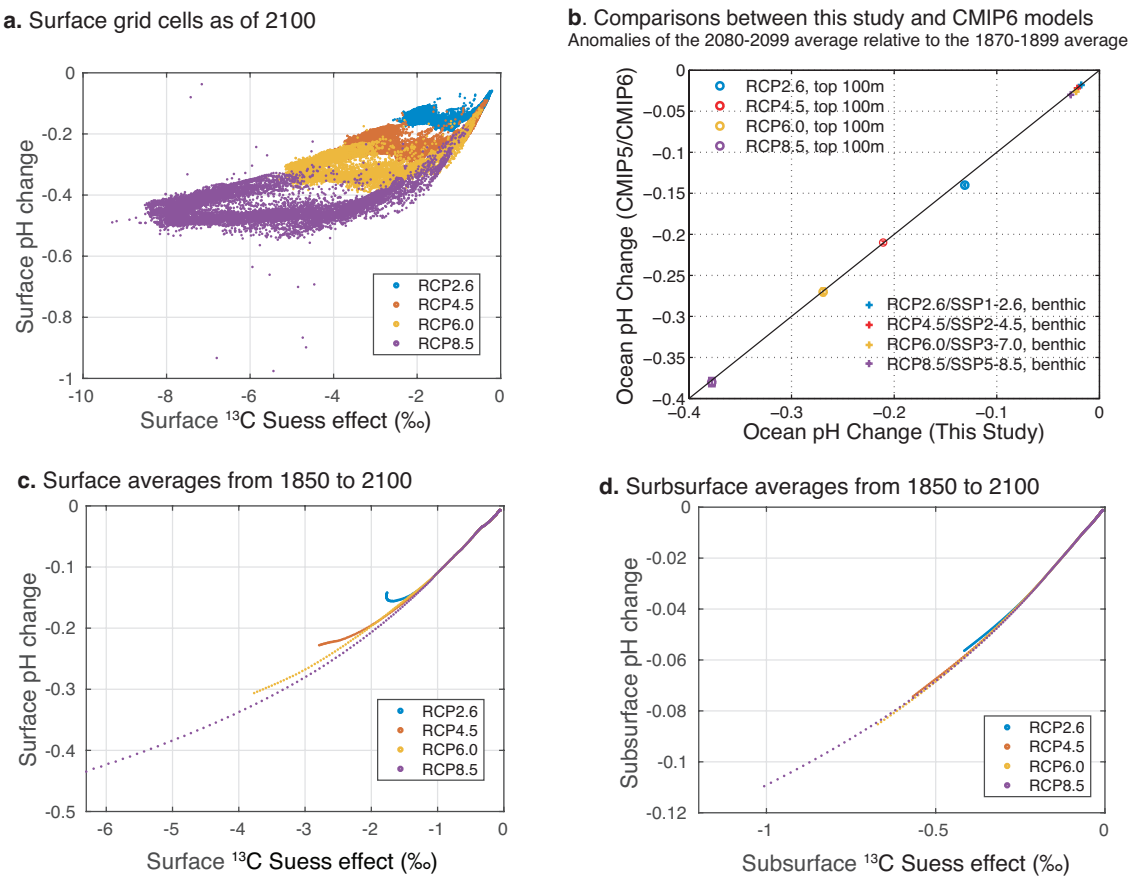

Supplementary Figure 6 Simulated oceanic ^{13}C Suess effects and pH changes. (a) Simulated ^{13}C Suess effects are compared with simulated pH changes for all individual surface grid cells of the full model setup. A model year of 2100 is chosen from the projections under RCP2.6 (blue), RCP4.5 (red), RCP6.0 (yellow), and RCP8.5 (purple). (b) Globally averaged simulated pH changes (anomalies of the 2080-2099 average relative to the 1870-1899 average) from the full model setup are compared with those from CMIP5 models [40,41] for the top 100m values and from CMIP6 models [40] for the benthic averaged values. Open circles show the averages for the top 100 m and crosses show the averages for the benthic grid cells (the bottom layer of the ocean model). The inter-model spreads are shown in error bars for the CMIP5/CMIP6 model estimates, although they are small and hence not visible. (c) Simulated surface-averaged ^{13}C Suess effects are compared with simulated surface-averaged pH changes from a model year of 1850 (dots in the upper right) to 2100 (dots in the lower left). (d) Same as (c) except that the subsurface averages are shown.

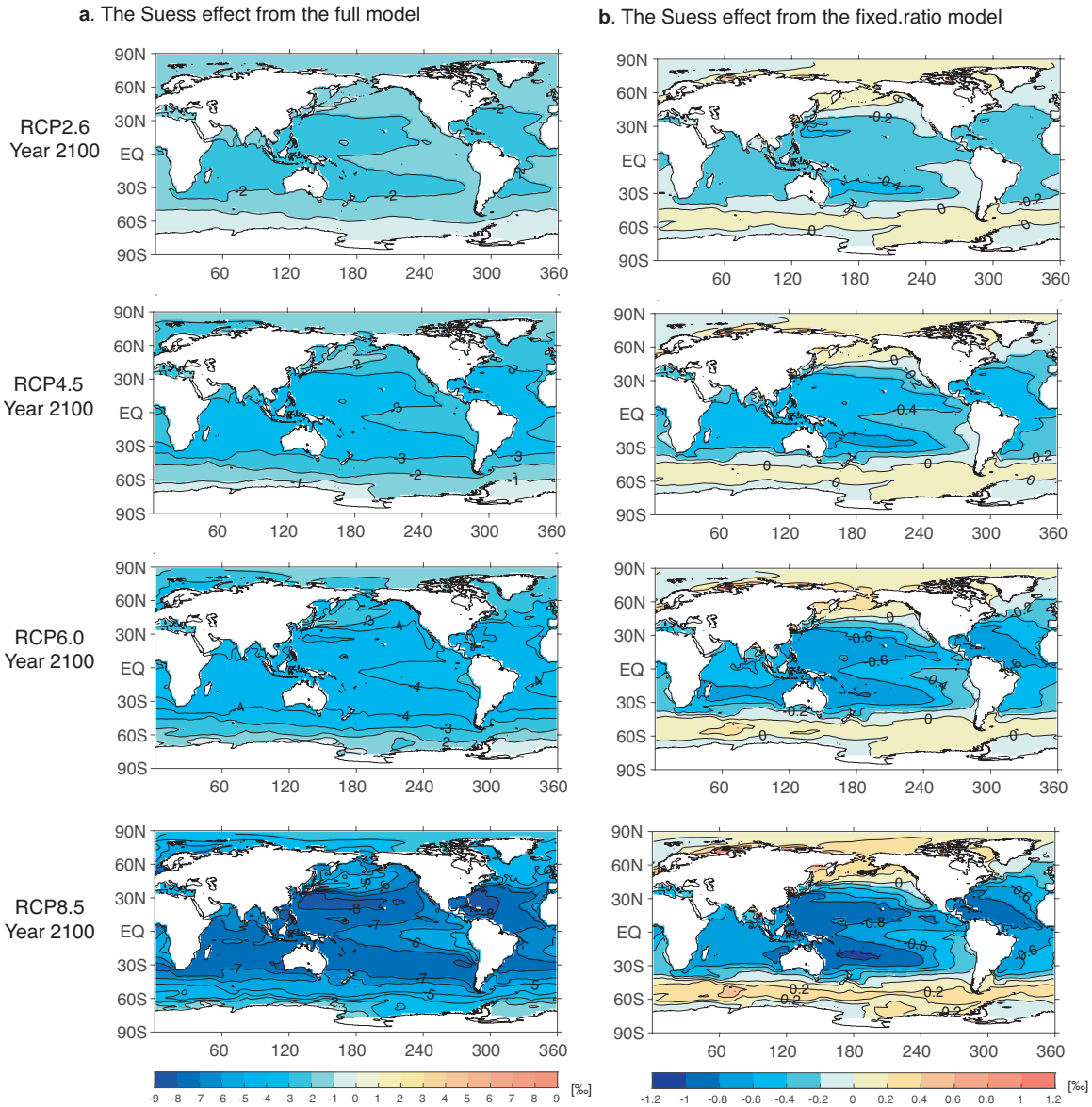

Supplementary Figure 7 Surface ocean ^{13}C Suess effect. The estimates as of 2100 are shown in the first (RCP2.6), second (RCP4.5), third (RCP6.0), and fourth (RCP8.5) rows. (a) The Suess effect from the full model setup where both atmospheric CO_2 and $\delta^{13}C$-CO_2 change over time. (b) The Suess effect from the fixed atmospheric $\delta^{13}C$-CO_2 setup where only atmospheric CO_2 changes while the $\delta^{13}C$-CO_2 remains fixed at a preindustrial value of -6.5 ‰. We also turn off the kinetic fractionations during air-sea CO_2 exchange and the CO_2 dependent photosynthetic fractionations in order to focus on the effect of changing DIC on the natural component of $\delta^{13}C$-DIC.

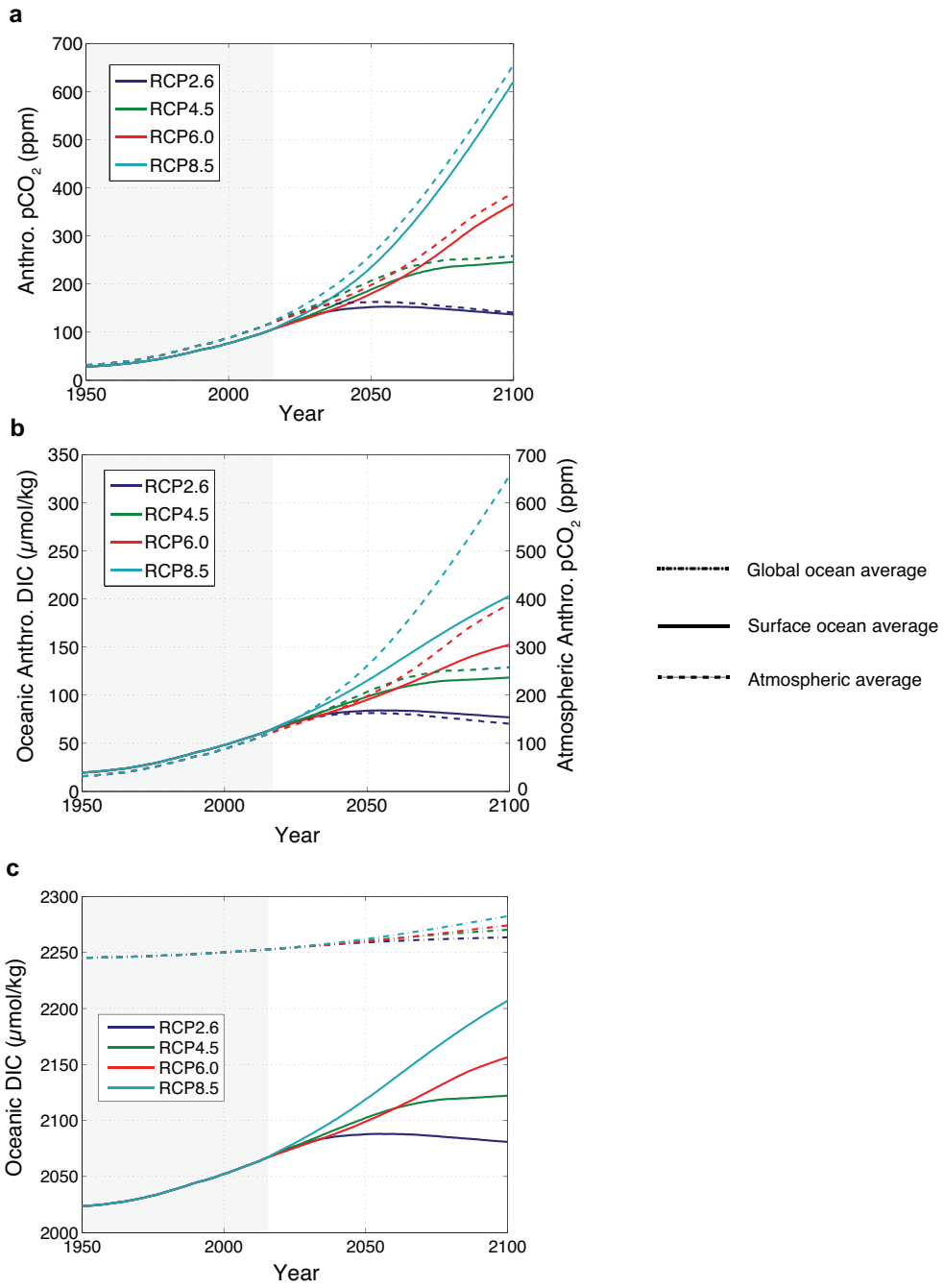

Supplementary Figure 8 Atmospheric and oceanic pCO_2 and DIC with time. (a) The globally averaged ocean surface (estimated in this study) and atmospheric (observed by ref. [39]) pCO_2 from 1950 to 2018 (shade background) are combined with the projected values from 2019 to 2100. Deviations from the respective preindustrial values are shown. Four different colors indicate different CO_2 emission scenarios of RCP2.6 (purple), RCP4.5 (green), RCP6.0 (red), RCP8.5 (blue). Dashed lines show the atmospheric pCO_2 and solid lines show the surface ocean averaged pCO_2. (b) Same as (a) except that the solid lines show the surface ocean averaged DIC. The Y-axis on the left is for DIC and the Y-axis on the right is for atmospheric pCO_2. (c) The surface-averaged DIC concentrations are shown in solid lines whereas the subsurface (below a depth of 74 m) averaged DIC concentrations are shown in dashed-dotted lines.

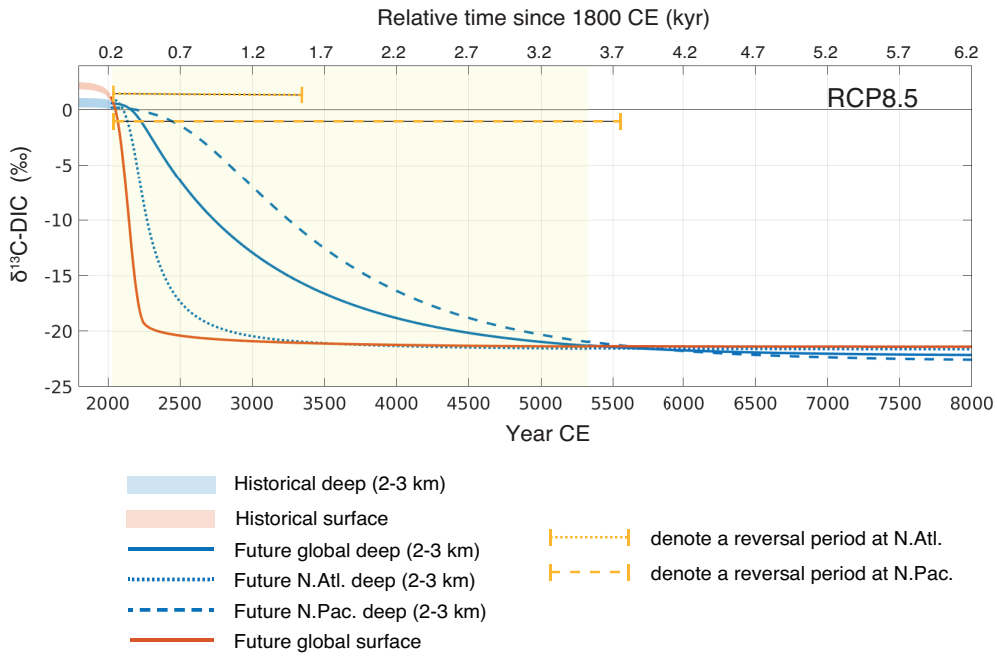

Supplementary Figure 9 δ^{13}C-DIC changes during industrial times under an extended RCP8.5. Estimates of surface and deep ocean (2-3km) δ^{13}C-DIC averaged over the global ocean are shown. The Monte Carlo experiment-based estimates from 1800 to 2018 are combined with a projection from 2019 to 8000. The atmospheric CO_2 and δ^{13}C-CO_2 are assumed to remain constant after 2500 at the values of 2500. The time period over which the globally averaged surface δ^{13}C-DIC falls below the deep ocean global average is highlighted as yellow shading. The duration of the vertical gradient reversal is sensitive to the geographic locations, as shown for the North Atlantic (N.Atl., north of 20°N) and the North Pacific (N.Pac., north of 20°N).

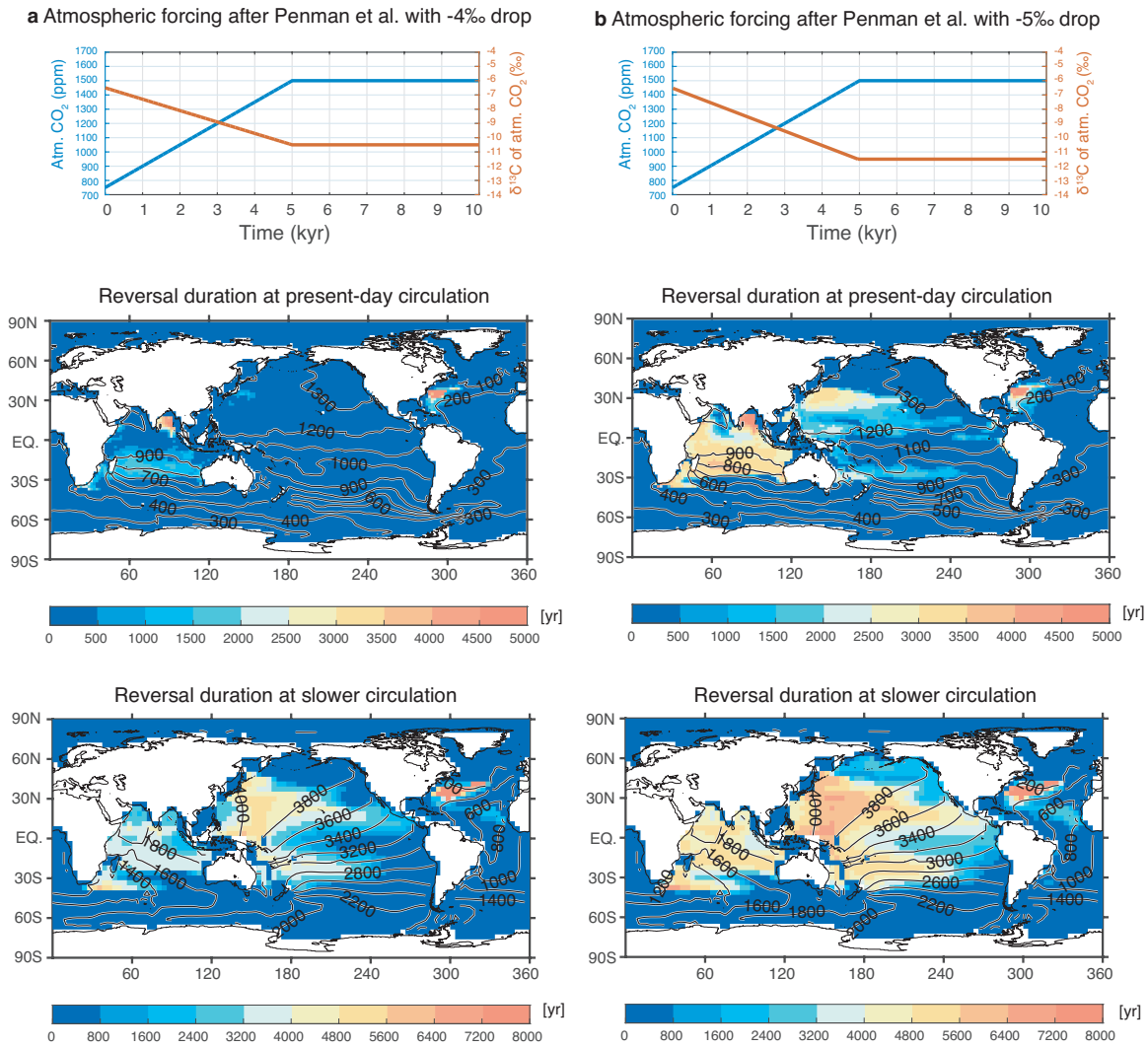

Supplementary Figure 10 Simulated responses of oceanic δ^{13}C-DIC to atmospheric CO_2 forcing. (a) The top panel shows an estimated change in atmospheric CO_2 (blue) for the PETM onset, following ref. [42]. The atmospheric δ^{13}C-CO_2 (red) is assumed to be linearly scaled with atmospheric CO_2 starting from a zero excursion at a time zero and a maximum excursion of -4 ‰ in 5 kyr. The middle panel shows the oceanic response when the present-day ocean circulation model is used for the simulation. Color shading shows the temporal duration over which the averaged δ^{13}C-DIC at 2-3 km depths lies above the local surface δ^{13}C-DIC by more than 0.5 ‰. Contour lines show the averaged ventilation ages at 2-3 km depths. The bottom panel is same as the middle panel except that an ocean model with slower ventilation rates, taken from Kwon, et al. [43], is used. (b) Same as (a) except that the atmospheric δ^{13}C-CO_2 is assumed to be linearly scaled with atmospheric CO_2 starting from a zero excursion at a time zero and a maximum excursion of -5 ‰ in 5 kyr.

Supplementary Table 1. Input Parameter Values Used for the Monte Carlo Simulations

Input parameters	The "full" model setup for future projections	The Monte Carlo experiment for industrial era simulations	References
Globally-averaged air-sea CO_2 transfer velocity (cm/hr)	15.1	[13.0 17.0]	[4-7]
SST for the equilibrium fractionation of $^{13}C/^{12}C$ during air-sea CO_2 exchange	HadISST1	HadISST1 ERSSTv5 COBE-SST2	[21] [22] [44]
Equilibrium fractionation factors during air-sea CO_2 exchange	$\alpha_{DIC\leftarrow g} = 1.4\times10^{-5}\cdot T\cdot f_{CO3} - 1.05\times10^{-4}\cdot T + 1.01053$	$\alpha_{DIC\leftarrow g} = 1.4\times10^{-5}\cdot T\cdot f_{CO3} - 1.05\times10^{-4}\cdot T + (1.01053\pm0.00005)$	[20]
Photosynthetic fractionation factors	$\alpha_{OC\leftarrow aq} = -0.00935\cdot log_{10}([CO_2]) + 0.99626$	$\alpha_{OC\leftarrow aq} = -0.00935\cdot log_{10}([CO_2]) + 0.99626$ $\alpha_{OC\leftarrow aq} = -0.017\cdot log_{10}([CO_2]) + 1.0034$ $\alpha_{OC\leftarrow aq} = -0.01203\cdot log_{10}([CO_2]) + 1.00119$	[24] [25] [26]
The $\delta^{13}C$ values for riverine carbon inputs (‰)	DOC: -27 POC: -35 DIC: -15	DOC: -27±2 POC: -35±2 DIC: -15±2	[27,28]
Non-riverine carbon inputs (GtC/yr)	0	[0 1.4]	[16] [15]
Sedimentary burial of inorganic carbon (GtC/yr)	0.2	[0.1 0.3][a]	[17,18]
Preindustrial $\delta^{13}C$ value for atmospheric CO_2 (‰)	-6.5	[-6.5 -6.3][b]	[34]
Ocean circulation model with different mixing parameterization	ω2	CTL, ω2, ω4, $K_{I,2000}$, $K_{I,600}$, $K_{V,1.5}$, $\gamma_{0.27}$, P1, P2, P3	[31]

[a]Because our model assumes a steady-state during the preindustrial era, the inorganic carbon burial implemented in the model is a portion that is balanced by terrestrial carbon inputs. Therefore, the previously reported range of 0.2-0.4 GtC/yr is adjusted to a balanced sink of 0.1-0.3 GtC/yr.
[b]The range is bracketed by a preindustrial mean value and a value as of 1780, both of which are constrained by Rubino, et al. [34].
[c]The suite of ocean circulation models have slightly different temperature and salinity as well as different ocean mixing, leading to different surface productivity and carbonate chemistry in seawater.

Supplementary References

1 Kwon, E. Y. *et al.* Stable carbon isotopes suggest large terrestrial carbon inputs to the global ocean. *Global Bigeochem. Cycles* **35**, e2020GB006684, doi:10.1029/2020GB006684 (2021).

2 Wanninkhof, R. Relationship between wind-speed and gas exchange over the ocean. *J. Geophys. Res.* **97**, 7373-7382, doi:Doi 10.1029/92jc00188 (1992).

3 Najjar, R. G. *et al.* Impact of circulation on export production, dissolved organic matter, and dissolved oxygen in the ocean: Results from Phase II of the Ocean Carbon-cycle Model Intercomparison Project (OCMIP-2). *Global Biogeochemical Cycles* **21**, doi:10.1029/2006gb002857 (2007).

4 Naegler, T., Ciais, P., Rodgers, K. & Levin, I. Excess radiocarbon constraints on air-sea gas exchange and the uptake of CO_2 by the oceans. *Geophys. Res. Lett.* **33**, L11802, doi:10.1029/2005GL025408 (2006).

5 Sweeney, C. *et al.* Constraining global air–sea gas exchange for CO_2 with recent bomb ^{14}C measurements. *Global Biogeochem. Cycles* **21**, doi:10.1029/2006GB002784 (2007).

6 Graven, H. D., Gruber, N., Key, R., Khatiwala, S. & Giraud, X. Changing controls on oceanic radiocarbon: New insights on shallow-to-deep ocean exchange and anthropogenic CO_2 uptake. *J. Geophys. Res.* **117**, C10005, doi:10.1029/2012JC008074 (2012).

7 Wanninkhof, R. *et al.* Global ocean carbon uptake: magnitude, variability and trends. *Biogeosciences* **10**, 1983-2000, doi:10.5194/bg-10-1983-2013 (2013).

8 Kwon, E. Y. & Primeau, F. Optimization and sensitivity of a global biogeochemistry ocean model using combined in situ DIC, alkalinity, and phosphate data. *J. Geophys. Res.* **113**, doi:10.1029/2007JC004520 (2008).

9 Lauvset, S. K. *et al.* A new global interior ocean mapped climatology: the $1° \times 1°$ GLODAP version 2. *Earth System Science Data* **8**, 325-340, doi:10.5194/essd-8-325-2016 (2016).

10 Garcia, H. E. *et al.* World Ocean Atlas 2018. 35 pp (2018).

11 Manizza, M. *et al.* Modeling transport and fate of riverine dissolved organic carbon in the Arctic Ocean. *Global Biogeochemical Cycles* **23**, doi:10.1029/2008GB003396 (2009).

12 Mayorga, E. *et al.* Global Nutrient Export from WaterSheds 2 (NEWS 2): Model development and implementation. *Environ. Modell. Softw.* **25**, 837-853, doi:10.1016/j.envsoft.2010.01.007 (2010).

13 Lamarque, J. F. *et al.* Historical (1850–2000) gridded anthropogenic and biomass burning emissions of reactive gases and aerosols: methodology and application. *Atmospheric Chemistry and Physics* **10**, 7017-7039, doi:10.5194/acp-10-7017-2010 (2010).

14 Meybeck, M. & Ragu, A. GEMS-GLORI world river discharge database. (Laboratoire de Géologie Appliquée, Université Pierre et Marie Curie, Paris, France, PANGAEA, 2012).

15 Duarte, C. M. Reviews and syntheses: Hidden forests, the role of vegetated coastal habitats in the ocean carbon budget. *Biogeosciences* **14**, 301-310, doi:10.5194/bg-14-301-2017 (2017).

16 Szymczycha, B., Maciejewska, A., Winogradow, A. & Pempkowiak, J. Could submarine groundwater discharge be a significant carbon source to the southern Baltic Sea? *Oceanologia* **56**, 327-347 (2014).
17 Sarmiento, J. L. & Sundquist, E. T. Revised budget for the oceanic uptake of anthropogenic carbon dioxide. *Nature* **356**, 589-593 (1992).
18 Milliman, J. D. Production and accumulation of calcium carbonate in the ocean: Budget of a nonsteady state. *Global Biogeochem. Cycles* **7**, 927-957, doi:Doi 10.1029/93gb02524 (1993).
19 Schmittner, A. *et al.* Biology and air-sea gas exchange controls on the distribution of carbon isotope ratios ($\delta^{13}C$) in the ocean. *Biogeosciences* **10**, 5793–5816 (2013).
20 Zhang, J., Quay, P. D. & Wilbur, D. O. Carbon-isotope fractionation during gas-water exchange and dissolution of CO_2. *Geochim. Cosmochim. Ac.* **59**, 107-114 (1995).
21 Rayner, N. A. *et al.* Global analyses of sea surface temperature, sea ice, and night marine air temperature since the late nineteenth century. *Journal of Geophysical Research-Atmospheres* **108**, 4407, doi:10.1029/2002JD002670 (2003).
22 Huang, B. Y. *et al.* Extended reconstructed sea surface temperature, version 5 (ERSSTv5): Upgrades, validations, and intercomparisons. *J. Clim.* **30**, 8179-8205, doi:10.1175/JCLI-D-16-0836.1 (2017).
23 Hirahara, S., Ishii, M. & Fukuda, Y. Centennial-scale sea surface temperature analysis and its uncertainty. *J. Clim.* **27**, 57-75, doi:10.1175/JCLI-D-12-00837.1 (2014).
24 Goericke, R. & Fry, B. Variations of marine plankton $\delta^{13}C$ with latitude, temperature, and dissolved CO_2 in the world ocean. *Global Bigeochem. Cycles* **8**, 85-90 (1994).
25 Popp, B. N., Takigiku, R., Hayes, J. M., Louda, J. W. & Baker, E. W. The post-Paleozoic chronology and mechanism of ^{13}C depletion in primary marine organic matter. *Am. J. Sci.* **289**, 436-454, doi:10.2475/ajs.289.4.436 (1989).
26 Freeman, K. H. & Hayes, J. M. Fractionation of carbon isotopes by phytoplankton and estimates of ancient CO_2 levels. *Global Bigeochem. Cycles* **6**, 185-198, doi:10.1029/92gb00190 (1992).
27 Peterson, B. J. & Fry, B. Stable isotopes in eco-system studies. *Ann. Rev. Ecol. Syst.* **18**, 293-320 (1987).
28 Marwick, T. R. *et al.* The age of river-transported carbon: A global perspective *Global Bigeochem. Cycles* **29**, 122-137, doi:10.1002/2014GB004911 (2015).
29 Maher, D. T., Santos, I. R., Golsby-Smith, L., Gleeson, J. & Eyre, B. D. Groundwater-derived dissolved inorganic and organic carbon exports from a mangrove tidal creek: The missing mangrove carbon sink? *Limnol. Oceanogr.* **58**, 475-488 (2013).
30 Abril, G. *et al.* Export of ^{13}C-depleted dissolved inorganic carbon from a tidal forest bordering the Amazon estuary. *Estuar Coast Shelf Sci.* **129**, 23-27 (2013).
31 DeVries, T. The oceanic anthropogenic CO_2 sink: Storage, air-sea fluxes, and transports over the industrial era. *Global Biogeochem. Cycles* **28**, 631-647, doi:10.1002/2013GB004739 (2014).

32 DeVries, T. & Primeau, F. Dynamically and observationally constrained estimates of water-mass distributions and ages in the global ocean. *J. Phys. Oceanogr.* **41**, 2381-2401, doi:10.1175/Jpo-D-10-05011.1 (2011).
33 DeVries, T. & Holzer, M. Radiocarbon and helium isotope constraints on deep ocean ventilation and mantle-^{3}He sources. *Journal of Geophysical Research: Oceans* **124**, 3036-3057, doi:10.1029/2018JC014716 (2019).
34 Rubino, M. *et al.* A revised 1000 year atmospheric $\delta^{13}C$-CO_2 record from Law Dome and South Pole, Antarctica. *J. Geophys. Res.* **118**, 8482-8499 (2013).
35 Holden, P. B. *et al.* Controls on the spatial distribution of oceanic $\delta^{13}C_{DIC}$. *Biogeosciences* **10**, 1815-1833 (2013).
36 Danabasoglu, G. *et al.* The Community Earth System Model Version 2 (CESM2). *Journal of Advances in Modeling Earth Systems* **12**, e2019MS001916, doi:10.1029/2019MS001916 (2020).
37 Rodgers, K. B. *et al.* Ubiquity of human-induced changes in climate variability. *Earth System Dynamics* **12**, 1393-1411, doi:10.5194/esd-12-1393-2021 (2021).
38 Schmittner, A. *et al.* Calibration of the carbon isotope composition ($\delta^{13}C$) of benthic foraminifera. *Paleoceanography* **32**, 512–530, doi:10.1002/2016PA003072 (2017).
39 Keeling, C. D. *et al.* in *A History of Atmospheric CO_2 and its effects on Plants, Animals, and Ecosystems* (eds J.R. Ehleringer, T.E. Cerling, & Dearing.M.D.) (Springer Verlag, 2005).
40 Kwiatkowski, L. *et al.* Twenty-first century ocean warming, acidification, deoxygenation, and upper-ocean nutrient and primary production decline from CMIP6 model projections. *Biogeosciences* **17**, 3439-3470, doi:10.5194/bg-17-3439-2020 (2020).
41 Bopp, L. *et al.* Multiple stressors of ocean ecosystems in the 21st century: projections with CMIP5 models. *Biogeosciences* **10**, 6225-6245, doi:10.5194/bg-10-6225-2013 (2013).
42 Penman, D. E. & Zachos, J. C. New constraints on massive carbon release and recovery processes during the Paleocene-Eocene Thermal Maximum. *Environmental Research Letters* **13**, doi:10.1088/1748-9326/aae285 (2018).
43 Kwon, E. Y., Sarmiento, J. L., Toggweiler, J. R. & DeVries, T. The control of atmospheric pCO_2 by ocean ventilation change: The effect of the oceanic storage of biogenic carbon. *Global Bigeochem. Cycles* **25**, doi:10.1029/2011GB004059 (2011).
44 Hirahara, S., Ishii, M. & Fukuda, Y. Centennial-scale sea surface temperature analysis and its uncertainty. *J. Clim.* **27**, doi:10.1175/JCLI-D-12-00837.1 (2014).